*Acta Oceanol. Sin.*, 2024, Vol. 43, No. 1, P. 22–34
https://doi.org/10.1007/s13131-023-2271-x
http://www.aosocean.com
E-mail: ocean2@hyxb.org.cn

# The variation in basal channels and basal melt rates of Pine Island Ice Shelf

Mingliang Liu[1, 2], Zemin Wang[1, 2], Baojun Zhang[1, 2]*, Xiangyu Song[3, 4], Jiachun An[1, 2]

[1] Chinese Antarctic Center of Surveying and Mapping, Wuhan University, Wuhan 430079, China

[2] Key Laboratory of Polar Environment Monitoring and Public Governance (Wuhan University), Ministry of Education, Wuhan 430079, China

[3] School of Civil Engineering, Shijiazhuang Tiedao University, Shijiazhuang 050043, China

[4] Key Laboratory of Roads and Railway Engineering Safety Control (Shijiazhuang Tiedao University), Ministry of Education, Shijiazhuang 050043, China

Received 11 August 2023; accepted 20 October 2023



**Abstract**

In recent years, there has been a significant acceleration in the thinning, calving and retreat of the Pine Island Ice Shelf (PIIS). The basal channels, results of enhanced basal melting, have the potential to significantly impact the stability of the PIIS. In this study, we used a variety of remote sensing data, including Landsat, REMA DEM, ICESat-1 and ICESat-2 satellite altimetry observations, and IceBridge airborne measurements, to study the spatiotemporal changes in the basal channels from 2003 to 2020 and basal melt rate from 2010 to 2017 of the PIIS under the Eulerian framework. We found that the basal channels are highly developed in the PIIS, with a total length exceeding 450 km. Most of the basal channels are ocean-sourced or groundingline-sourced basal channels, caused by the rapid melting under the ice shelf or near the groundingline. A raised seabed prevented warm water intrusion into the eastern branch of the PIIS, resulting in a lower basal melt rate in that area. In contrast, a deep-sea trough facilitates warm seawater into the mainstream and the western branch of the PIIS, resulting in a higher basal melt rate in the main-stream, and the surface elevation changes above the basal channels of the mainstream and western branch are more significant. The El Niño event in 2015–2016 possibly slowed down the basal melting of the PIIS by modulating wind field, surface sea temperature and depth seawater temperature. Ocean and atmospheric changes were driven by El Niño, which can further explain and confirm the changes in the basal melting of the PIIS.

**Key words:** Pine Island Ice Shelf, basal channel, basal melt rate, digital elevation models (DEMs), satellite altimetry

**Citation:** Liu Mingliang, Wang Zemin, Zhang Baojun, Song Xiangyu, An Jiachun. 2024. The variation in basal channels and basal melt rates of Pine Island Ice Shelf. Acta Oceanologica Sinica, 43(1): 22–34, doi: 10.1007/s13131-023-2271-x

## 1 Introduction

An ice shelf is the floating extension of the ice sheet over the sea, supporting the stability of the ice sheet. Thinning of an ice shelf will weaken its support, leading to accelerated mass loss of ice sheet and contributing the rise of sea level (Alley et al., 2005; Paolo et al., 2015; Rignot et al., 2019). Currently, basal melting is the main pathway for mass loss of the Antarctic ice shelf and the primary driving factor for mass loss of the Antarctic ice sheet (Pritchard et al., 2012; Shepherd et al., 2018; Liu et al., 2015). Basal channels located at the bottom of floating ice shelves can cause uneven basal melting (Shepherd et al., 2003; Fricker and Padman, 2012; Rignot and Steffen, 2008; Bindschadler et al., 2011; McGrath et al., 2012; Logan et al., 2013; Chartrand and Howat, 2020), thereby affecting the stability of the ice shelves structure (Jacobs et al., 1996; Bintanja et al., 2013; Vaughan et al., 2012; Alley et al., 2016; Wang et al., 2020). Basal channels can be formed by various mechanisms, such as the intrusion of circumpolar deep water (CDW) and surface seawater, drainage at the base of ice sheets, undulating bedrock topography upstream of groundingline. Alley et al. (2016) classified the basal channels into three categories based on whether they originate from the groundingline and correspond to modeled subglacial outflow: (1) ocean-sourced basal channels neither originate from the groundingline nor correspond to modeled subglacial outflow; (2) subglacial-sourced basal channels originate from the groundingline and corresponding to modelled subglacial outflow; (3) groundingline-sourced basal channels originate from the groundingline but do not correspond to modelled subglacial outflow. This provides an important reference for future research on the development of basal channels.

Currently, ice-penetrating radar technology and underwater ice cavity detection technology cannot achieve long-term observation of the basal channels (Vaughan et al., 2012). However, during the formation of the basal channels, the ice shelf itself undergoes creep under hydrostatic, resulting in a depression on surface of the ice shelves corresponding to the location of the basal channels (Bindschadler et al., 2011; Alley et al., 2016; Wang et al., 2020). Therefore, most of studies depicted the changes of the basal channels mostly depends on the inversion of remote sensing or satellite altimetry data (Alley et al., 2016; Chartrand

Foundation item: The National Natural Science Foundation of China under contract Nos 41941010 and 42006184; the Fundamental Research Funds for the Central Universities under contract No. 2042022kf1068.
*Corresponding author, E-mail: bjzhang@whu.edu.cn

and Howat, 2020; Wang et al., 2020). Further research is required to thoroughly describe the thinning and melting of ice shelves by studying the long-term temporal and spatial changes of the basal channels.

The Amundsen Sea coastal ice shelves in the West Antarctic had experienced significant acceleration and thinning, and making a significant contribution to sea level rise (Paolo et al., 2015; Pritchard et al., 2012; Shepherd et al., 2018). The Pine Island Ice Shelf (PIIS) is one of the major ice shelves in the West Antarctic. The stability of the PIIS continues to weaken, reducing its support for upstream glaciers and further accelerating glacial overflow, making it the region with the most significant mass loss for the Antarctic ice sheet (Paolo et al., 2015; Pritchard et al., 2012; Liu et al., 2015). The basal melting of the PIIS was mainly driven by the modified circumpolar deep water (mCDW) from the Amundsen Sea (Wåhlin et al., 2010; Walker et al., 2013; De Rydt et al., 2014; Dutrieux et al., 2014). Several simulation studies shown that the accelerated melt of the PIIS is due to the basal melting concentrated near the groundingline and the loss of bottom traction caused by groundingline retreat (Payne et al., 2004; Joughin et al., 2010, 2019; Favier et al., 2014). Accelerated basal melting near the groundingline has affected the evolution of the groundingline and leads to sea-level rise in the future (Favier et al., 2014; Cornford et al., 2015; Joughin et al., 2014; Nias et al., 2016; Seroussi et al., 2017).

PIIS's groundingline was probably engaged in an unstable 40 km retreat (Favier et al., 2014), and the mass loss will exceed 100 Gt/a equivalent to 3.5–10 mm eustatic sea-level rise over the next 20 a (Favier et al., 2014). Mean basal melt rates of the PIIS were 82–93 Gt/a from 2008 to 2015, with basal melt rates of 200–250 m/a within large channels near the groundingline, 10–30 m/a over the main shelf, and 0–10 m/a over the northeast shelf and southwest shelf, with the notable exception of a small area with rates of 50–100 m/a near the groundingline of a fast-flowing tributary on the southwest shelf (Shean et al., 2019). Enhanced basal melting along narrow basal channels play an important role in the formation of some basal and surface crevasses, greatly weakening the structural stability of the PIIS (Vaughan et al., 2012). The melt rate at the basal channel apex of the PIIS was 0.06 m/d, while melt rate along the basal channel flanks was almost zero (Stanton et al., 2013).

The factors influencing ice shelf-ocean interaction and their physical mechanisms involved are very complex. In addition to the mCDW, local wind and the El Niño-Southern Oscillation (ENSO) also have an important impact on the basal melting and the development of basal channels of the PIIS. On timescales ranging from weeks to months, the primary factor regulating the basal melt rate of the PIIS was the response of the upper thermocline to local wind-forced changes in vertical Ekman velocity (Davis et al., 2018). The basal melt rates of the PIIS in 2012 decreased by over 50% compared to 2010, mainly due to the strong La Niña event (Dutrieux et al., 2014). 3D high-order model simulations have shown that enhancing ice shelf melting is the most important way in which climate change will affect ice shelf dynamics in the next 50 years, and it will rapidly accelerate the movement of glacier upstream of the groundingline by several hundred kilometers (Seroussi et al., 2014). In the future, the Pine Island Glacier will continue to accelerate, and even if ocean-induced basal melting reduces, it will remain a major contributor to sea level rise (Seroussi et al., 2014). Nevertheless, the role of the basal channels in the interaction between ice shelf and ocean requires further research. Owing to the limitations of the polar field environment, it is currently difficult to collect large-scale directly measured data on the basal channels of ice shelf, thus making it a challenge to comprehensively describe their development and evolution processes (Tang et al., 2008).

In the context of continuous global warming, the PIIS provides an ideal laboratory for studying the development and evolution of a basal channel and the driving factors of basal melting, and for exploring ocean–ice shelf interaction mechanism. Therefore, this study used the existing remote sensing to obtain the long-term time series of the basal channels and the surrounding basal melting of the PIIS, and to investigate their spatiotemporal changes and corresponding driving factors. We hope this work can further strengthen the understanding of the impact of the basal channels on the ice shelf stability.

## 2 Data and methods

### 2.1 *Landsat optical satellite remote sensing data*

The Landsat 7 satellite was launched in 1999. The satellite carries the Enhanced Thematic Mapper (ETM+) sensor, which passively senses the solar radiation reflected by the surface and the thermal radiation emitted by the surface. There are 8-band sensors that cover visible light ranging from infrared to different wavelength (Goward et al., 2001; Suga et al., 2003). The Landsat 8 satellite was launched in 2013. The satellite carries both a land imager and a thermal infrared sensor, which are used for data acquisition and monitoring in the visible light band and thermal infrared band respectively (Roy et al., 2014; Vermote et al., 2016). The 8-band panchromatic image data from the two satellites has the highest resolution of 15 m. This study used the resolution of 15 m panchromatic image data to identify the surface depression features corresponding to the basal channels.

### 2.2 *ICESat satellite altimetry data*

ICESat-1 and ICESat-2 were launched in 2003 and 2018 respectively. Their main tasks are to monitor elevation changes in the Antarctic and Greenland ice sheets, and to provide scientific data for studying the impact of polar ice sheet mass changes on sea level rise (Liu et al., 2020; Wang et al., 2013; Borsa et al., 2014; Fricker and Padman, 2006). The laser pulses from ICESat-1 that reach the ground form a spot with a diameter of about 70 m, with a distance of approximately 172 m between spots. The vertical resolution of the ground can reach 10 cm and the observation period is repeated every 91 d (Liu et al., 2020; Wang et al., 2013; Borsa et al., 2014; Fricker and Padman, 2006). The laser pulses from ICESat-2 that reach the ground form a spot with a diameter of about 17 m, with a distance of approximately 90 m between spots. The along-track resolution is about 0.7 m, and the observation period is repeated every 91 d, with the measurement accuracy of the annual ice sheet elevation change rates are better than or equal to 0.4 cm/a (Liu et al., 2020; Wang et al., 2013; Borsa et al., 2014; Fricker and Padman, 2006; Markus et al., 2017). This study used ICESat-1 (GLAH12, Version 34) and ICESat-2 (ATL06, Version 4) data to analyze the spatiotemporal changes of surface elevation above the basal channels from 2003 to 2009 and from 2018 to 2020.

### 2.3 *Reference Elevation Model of Antarctica (REMA) and digital elevation models (DEMs)*

The REMA is the first high-precision topographic map of the entire Antarctic (Howat et al., 2019). The images used to construct REMA are from four satellites, namely WorldView1, WorldView-2, WorldView-3, and GeoEye-1 (Howat et al., 2019). DEM is generated by the opensource and fully automated SETSM software package on the Blue Waters supercomputer at the National Center for Supercomputing Applications processing scene pairs (Noh and Howat, 2017). This product provides DEM of Antarc-

tica with spatial resolutions of 2 m, 8 m, 100 m, 200 m and 1 km (Noh and Howat, 2017). This study used REMA DEMs with spatial resolution of 2 m to analyze the temporal and spatial changes in the basal channels and the basal melt rates around the basal channels from 2010 to 2017. The systematic bias of REMA DEMs was corrected utilizing CryoSat-2 satellite altimetry data. The systematic bias was obtained by the difference between the DEM and the mean elevation in the same observation period inferred from CryoSat-2, and removed from the DEM. The detailed corrected process is divided into three steps: firstly, based on the month of collection of REMA DEM, the CryoSat-2 satellite altimetry data covering a small range of REMA DEM for a total of three months before and after each month were selected; then, the mean elevation of the area is calculated using CryoSat-2 satellite altimetry data, and the difference between the REMA DEM and the mean elevation is the deviation that exists in the REMA DEM; finally, subtract the deviation from REMA DEM to complete REMA DEM deviation correction.

### 2.4 *IceBridge*

IceBridge data was implemented by the US IceBridge (Operation IceBridge, OIB) program, using a variety of airborne equipment to measure Arctic and Antarctic ice shelves surface topography, bedrock topography, groundingline location, ice thickness, sea ice distribution and various other collected data (Kurtz and Farrell, 2011; Farrell et al., 2012). This study used IceBridge data to determine the presence and location of the basal channels in the PIIS.

### 2.5 *Assisted with data analysis*

In this study, we combined atmospheric and oceanic data to analyze the driving factors behind basal melting and development of basal channels of the PIIS, such as sea surface temperature (SST), wind, ENSO index, geopotential height, etc. We obtained the corresponding data from different institutions by referring to previous relevant research (Wang et al., 2020; Paolo et al., 2018). SST used data with a spatial resolution of 1° provided by the Met Office Hadley Center, version 3.1. The wind field data used monthly analyzed 10 m wind field data with a resolution of 0.25° from the European Center for Medium-Range Weather Forecasts (ECMWF) ERA5 (Hersbach et al., 2019). The ENSO index used the three-month moving mean data provided by the Climate Prediction Center. The geopotential height data used ERA5 reanalysis data provided by ECMWF with a resolution of 0.25° (Hersbach et al., 2019). groundingline used the MODIS Mosaic of Antarctica (MOA) 2009 groundingline products. The specific addresses for obtaining the above data will be added in the Data Availability Statement.

### 2.6 *Estimating basal melt rate*

We used 2-m high-resolution REMA DEMs to calculate the basal melt rate on an annual scale in the 10 km × 10 km area marked in Fig. 1 under the Eulerian framework from 2010 to 2017. The basal melt rate $W_b$ can be derived from the equation Eulerian (1) surface elevation change $\partial h/\partial t$ (Shepherd et al., 2003; Moholdt et al., 2014; Adusumilli et al., 2018; Liang et al., 2021) as

$$W_b = \frac{M_s}{\rho_i} - \left(\frac{\rho_w}{\rho_w - \rho_i}\right)\left(\frac{\partial h}{\partial t} - \frac{\partial h_w}{\partial t} - \frac{\partial H_a}{\partial t} + H_i \rho_i \frac{\partial}{\partial t}\left(\frac{1}{\rho_w}\right)\right) - \nabla \cdot (\boldsymbol{v} H_i), \quad (1)$$

where $h_w$ is the sea level height (m); $H_a$ is the firn air column (FAC) (m) with 27 km horizontal spacing from the RACMO 2.3p2

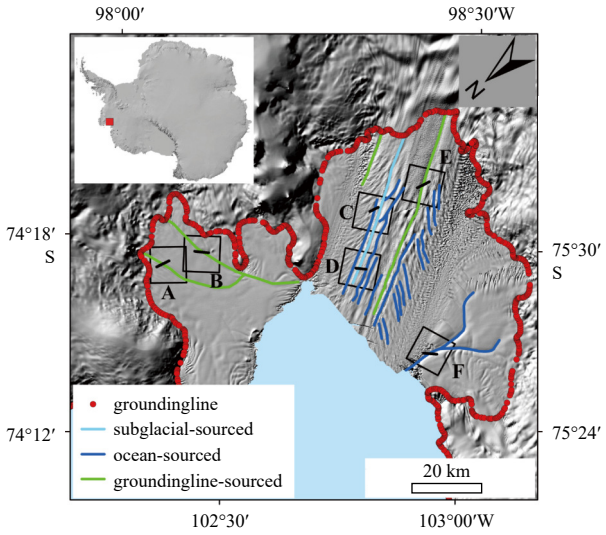


**Fig. 1.** The basal channels of the PIIS. Image is the REMA mosaic hillshade with a resolution of 100 m. The distribution of different types of the basal channels: blue represents ocean-sourced basal channel, green represents groundingline-sourced basal channel, and light blue represents subglacial-sourced basal channel. Black lines A–F mark the the basal channels where ICESat-1 and ICESat-2 pass through (named as channels A–F). The black square boxes A–F represent the 10 km × 10 km area around the basal channel (named as locations A–F). The range of SST acquisition is 75°S to 74°S, 102°W to 103°W.

(Ligtenberg et al., 2014), which is defined as the variation in thickness if the firn column is compressed to the density of glacier ice; $H_i$ is the ice equivalent thickness (m) with 500 m horizontal spacing (the thickness of an ice shelf assuming the whole column has the mean ice density) (Morlighem et al., 2018); $\rho_i$ and $\rho_w$ are the densities of ice [(917 ± 5) kg/m$^3$] and seawater [(1 028 ± 1) kg/m$^3$]; $M_s$ is the surface mass balance [SMB; kg/(m$^2$·a)] with 27 km horizontal spacing (van Wessem et al., 2018); $v$ is the ice surface velocity with 240 m horizontal spacing (m/a) (Gardner et al., 2019); $W_b$ is the basal melt rate (m/a); $\nabla \cdot (\boldsymbol{v} H_i)$ is the sum of ice advection $\boldsymbol{v} \cdot \nabla H_i$ and divergence $H_i \cdot \nabla \boldsymbol{v}$ (m/a); $\nabla H_i$ is the thickness gradient; and $\nabla \boldsymbol{v}$ is the velocity divergence (positive for extension). $\boldsymbol{v} \cdot \nabla H_i$ is used to correct the error caused by advection.

As ice shelves freely float on the ocean, changes in sea level height ($h_w$) and ocean density ($\rho_w$) can cause variations in the surface elevation of ice shelves. It has been reported that sea level has risen at mean rate of (3.6 ± 0.4) mm/a from 2005 to 2016 (WCRP Global Sea Level Budget Group, 2018). Changes in seawater density, which are affected by both salinity and temperature, result in a variation in elevation of ice shelves of about 2 mm/a (rising or falling) (Moholdt et al., 2014). Therefore, the influence of $h_w$ and $\rho_w$ can be ignored and Eq. (1) can be simplified as

$$W_b = \frac{M_s}{\rho_i} - \left(\frac{\rho_w}{\rho_w - \rho_i}\right)\left(\frac{\partial h}{\partial t} - \frac{\partial H_a}{\partial t}\right) - \nabla \cdot (\boldsymbol{v} H_i). \quad (2)$$

## 3 Basal channel change

### 3.1 *Basal channel identification*

In this study, the basal channels were identified by combining surface texture extracted from the remotely sensed data with IceBridge ice radar data, as the corresponding surface of the basal channel present depressions. First, this study used Landsat-7

and Landsat-8 optical remote sense images and REMA DEM to identify the surface depressions on the PIIS. Second, we used IceBridge ice radar data intersecting that intersect with these depressions to filter out the basal channels from these depressions. If there are also depressions on the bottom of the ice shelf corresponding to the locations of surface depressions, they are identified as the basal channels (Wang et al., 2020). Finally, the basal channels were divided into ocean-sourced basal channels, subglacial-sourced basal channels and groundingline-sourced basal channels. The geometric schematic diagram of the formation process of each type of the basal channel can refer to Fig. S5 of Alley et al. (2016). Note that the extracted basal channels were all verified by the IceBridge ice radar measurements. Some basal channels may not have been extracted due to the lack of IceBridge ice radar observations for validation.

We identified the distribution of the basal channels in the PIIS through visual interpretation based on the basal channel extraction method. Figure 1 shown the detailed distribution positions of the extracted basal channels in this study. The east branch of the PIIS only has groundingline-sourced basal channels, while the mainstream has three types of the basal channels, and the west branch only has ocean-sourced basal channels. The total length of the basal channels was about 455 km, of which the length of subglacial-sourced basal channels was about 44 km, the length of ocean-sourced basal channels was about 260 km, and the length of groundingline sourced basal channels was 151 km. In addition, there are some basal channels intersecting with the direction of ice velocity in the edge area of basal channel E. It is may be basal channels underneath the shelves cause ice thinning, resulting in the formation of the basal channels in the direction of intersecting ice velocity. Similar surface depression features were also observed in the edge area of the basal channels C and D, and they were not extracted due to the lack of data validation of IceBridge measured data.

In order to analyze the spatiotemporal changes of the basal channels in detail, we selected A–F six main sites of the basal channels as the main analysis objects according to the location and type of basal channels, the satellite altimetry data track and the coverage of 2 m resolution REMA DEM long time series. They were located in the east branch, west branch and mainstream of the PIIS, covering three types of the basal channels. Six specific locations (A–F in Fig. 1) were selected to study the spatial and temporal changes in the basal channels, for they had enough observations to form a time series. The locations A and B were located in the east branch of the PIIS, C, D, and E were located in the mainstream of the PIIS, and F was located on the west branch of the PIIS.

### 3.2 *Temporal and spatial variation in surface elevations above basal channel*

Due to the lack of measured data on the bottom of the Antarctic and Arctic ice shelves, it is impossible to monitor the actual shape changes of the basal channels for a long time. Analyzing the changes in surface elevation above the basal channels was a common way for studying the changes of the basal channels, as depressions are formed on the surface corresponding to the location of the basal channels (Chartrand and Howat, 2020; Alley et al., 2016; Wang et al., 2020).

Figure 2 showed the surface elevation changes above different the basal channels, according to the labeling order in Fig. 1. In order to display the results more clearly and intuitively, the data from different periods had been normalized. The altitude peaks on both sides of the depression area were selected as matching points, as the peak points were easier to match.

As shown in Fig. 2, the surface elevations above the basal channels A and B did not show significant changes from 2003 to 2020, indicating the basal channels at A and B were stable. The surface elevation above the basal channel C was relatively stable from 2007 to 2008, reached to the lowest in 2010, and there was a decrease in 2012 and 2015, with the most significant increase occurring in 2016. The surface elevation above the basal channel D was relatively stable from 2004 to 2007, and then decreased from 2010 to 2013 and increased from 2014 to 2015, and was at the lowest in 2016. The surface elevation above the basal channel E decreased from 2007 to 2015, and increased in 2016 and 2018. The surface elevation above the basal channel F reached its lowest point in 2007 and 2016, showed a large increase in 2014 and 2015, and was relatively stable in the remaining years.

## 4 Basal melt rate from high-resolution REMA DEMs

The location F is located at the front end of the west branch of the PIIS, where ice shelf calving occurred more frequently. The calving has a significant impact on the ice velocity and therefore has a very significant effect on the calculation of the basal melt rate (Bradley et al., 2022). Therefore, the basal melt rate around the location F was not calculated. Figure 3 showed the annual-scale maps of the basal melt rates for small areas A–E. Some maps might only cover a part of the 10 km × 10 km area in some periods because of the limited coverage of the corresponding 2-m resolution REMA DEMs.

As shown in Fig. 3, the basal melt rate in the east branch was significantly lower than in the mainstream. The basal melt rates of most areas around the locations A and B in the PIIS east branch were higher than 10 m/a, and its overall basal melt rate was 0~10 m/a, and the mean basal melt rate around the locations A and B was (3.89 ± 1.69) m/a which was consistent with results of Shean et al. (2019). The basal melt rates in PIIS mainstream were relatively larger, and the mean basal melt rate around the locations C, D, and E was (22.45 ± 15.45) m/a, and the basal melt rates of some areas were higher than 100 m/a. The basal melt rates in the basal channels were higher than other regions. Schmidt et al. (2023) observed the same phenomenon at Thwaites Glacier (Schmidt et al., 2023). They speculated that the higher lateral turbulent mixing and destabilizing rising glacial meltwater allowed warm water entering the sloped surfaces of the basal channels, thus promoting the basal melting (Gregg, 1987; Rosevear et al., 2022; Kerr and McConnochie, 2015).

In order to analyze temporal variation of basal melting, we compared the mean basal melt rate around the locations A, B, D and E from 2010 to 2017. In addition, the changes in ENSO, monthly mean speed of local wind and deep seawater temperature at 880–1 000 m depth during from 2010 to 2020, showed in Fig. 4. The mean annual basal melt rate of around the location E was discontinuous. In order to ensure a more intuitive presentation of the results, the missing annual mean basal melt rates were given the two-year mean basal melt rate.

As shown in Fig. 4a, the basal melt rate in the east branch was significantly lower than in the mainstream. The mean basal melt rates around the locations A and B were 0–6 m/a, around the location D was 0–60 m/a, and around the location E was 15–50 m/a. The mean basal melt rates around the locations A, B, D, and E first increased and then decreased from 2010/2011 to 2015/2016, and it was found that the ENSO index was relatively high in 2015/2016, indicating that an El Niño event occurred during this period. In addition, the monthly average wind speed and deep seawater temperature were significantly lower compared to other periods, which suppressed basal melting of the PIIS. In addition, we found that the ENSO index remained stable during other periods, while the monthly average wind speed exhibited a stable cyclic variation and the higher temperature of deep seawater

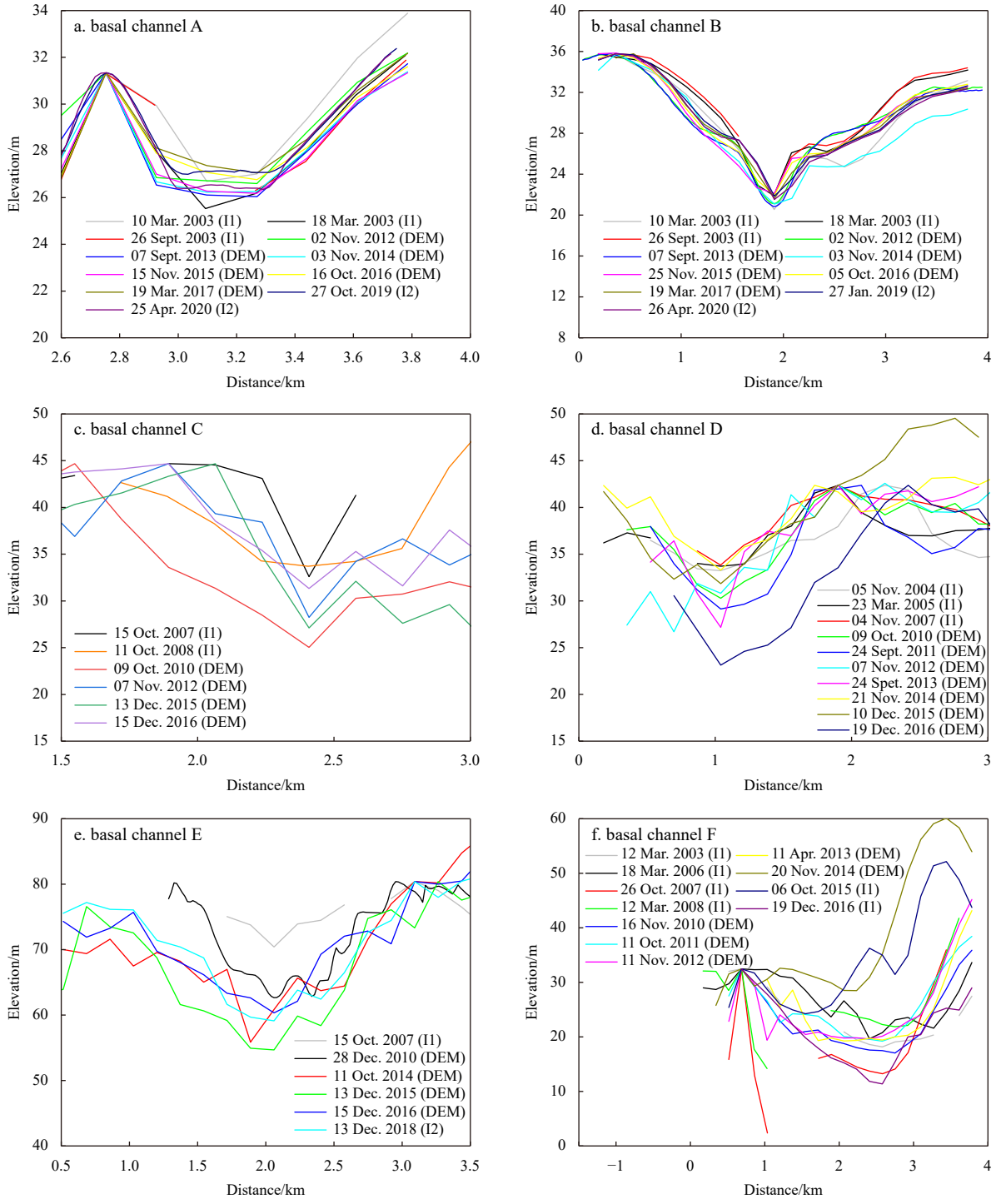


**Fig. 2.** The surface elevations along cross-section A–F from ICESat-1 (I1), ICESat-2 (I2) and REMA DEM above different basal channels of the PIIS. The tagging of each subplot is the same as the marks of the six specific locations A–F in Fig. 1.

contributed to a more severe basal melting of the PIIS compared to 2015–2016, and this higher melting rate has remained relatively stable. Therefore, it can be inferred that the abrupt change in the ENSO index (resulting from special natural events such as El Niño) will have an impact on the basal melting of the PIIS. Due to the lack of REMA DEMs in 2013 and 2014, the change in the annual basal melt rate around the location C from 2012–2013 to 2014–2015 cannot been estimated. But it was not difficult to speculate that it may have the same trend around the locations D and E, as the locations C, D and E are all located in the mainstream of PIIS and share similar environments.

## 5 Discussion

### 5.1 *East branch basal channels changes*

The refined seabed topography data shows that there is a raised continental shelf in the front of the east branch of the PIIS (Fig. 5). This raised seabed topography prevented the mCDW from entering the ice cavity of the PIIS east branch, resulting in a lower basal melt rate. Observations and simulations by Dutrieux et al. (2014) confirmed that the influence of ocean circulation on basal melting in the east branch of the PIIS was limited. This is why the changes in the basal channels at locations A and B were

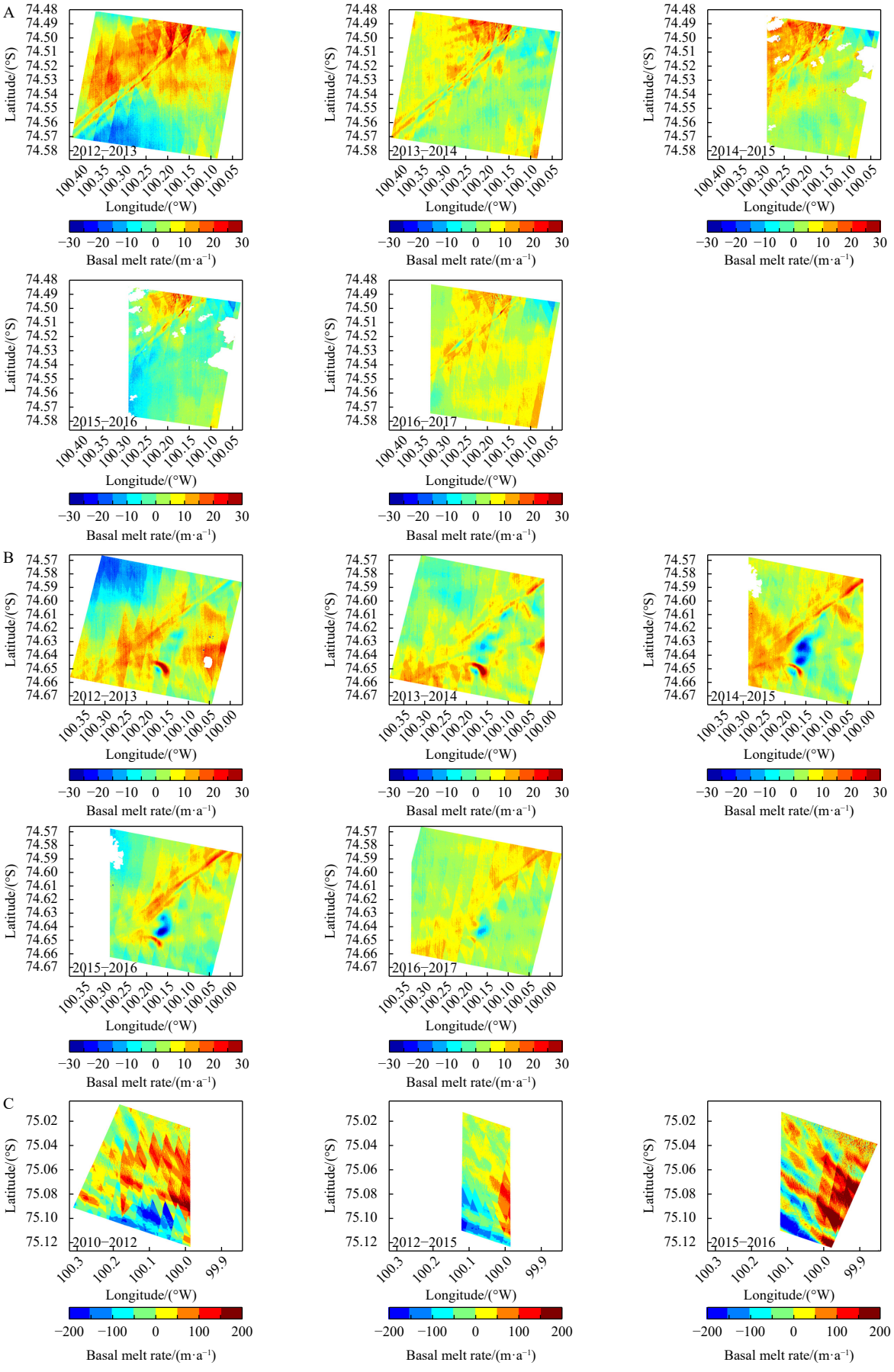
A
2012–2013
2013–2014
2014–2015
2015–2016
2016–2017
Latitude/(°S)
Longitude/(°W)
Basal melt rate/(m·a⁻¹)
B
2012–2013
2013–2014
2014–2015
2015–2016
2016–2017
C
2010–2012
2012–2015
2015–2016

**Fig. 3.**

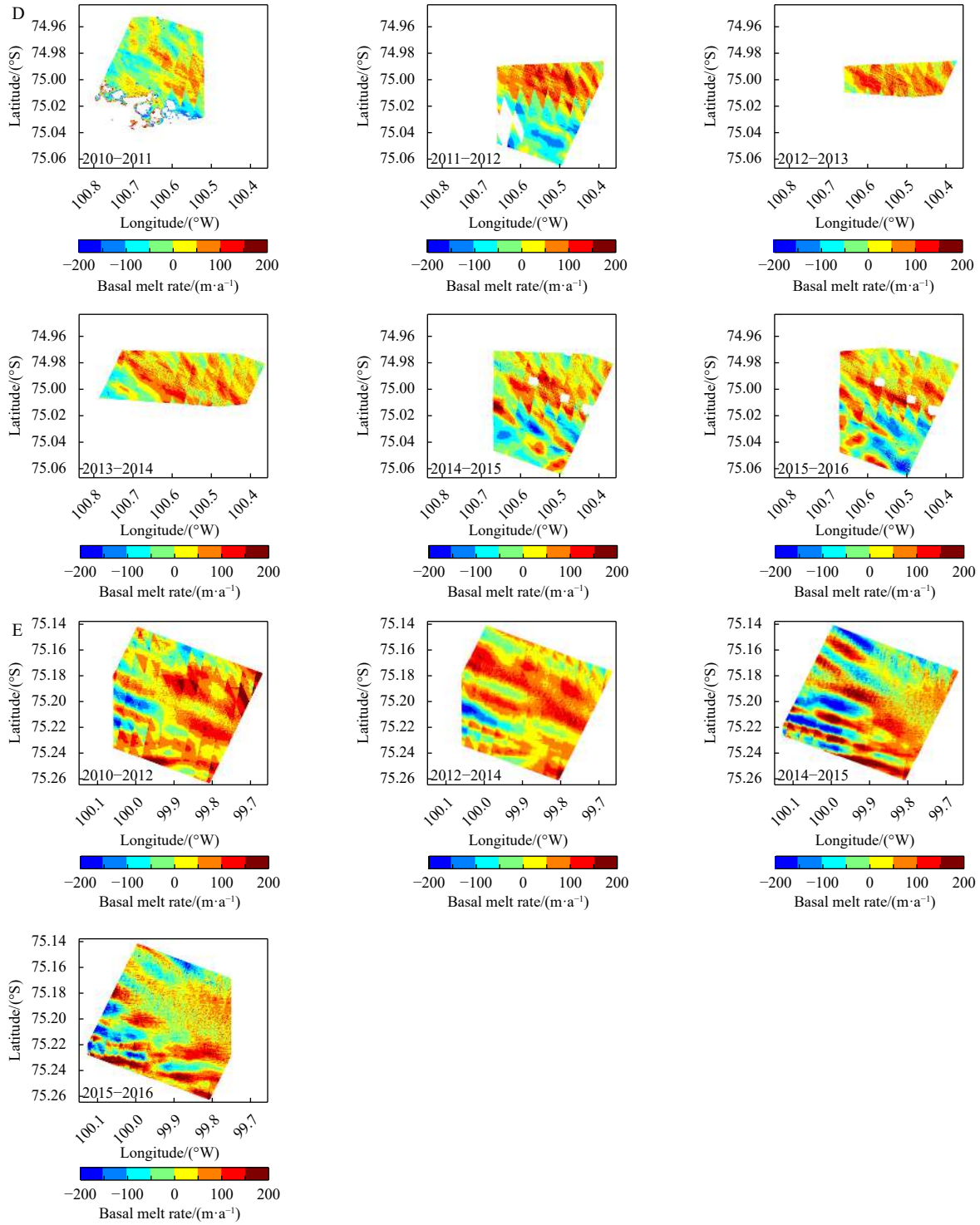


**Fig. 3.** The basal melt rate of 10 km × 10 km areas around the locations A–E. The irregular white areas were caused by missing data. The tagging of each subplot is the same as the marks of the five specific locations A–E in Fig. 1.

far less than the changes in the basal channels of the mainstream and the west branch of the PIIS.

### 5.2 *Mainstream basal channels changes*

Unlike the east branch, a sea trough in the front of mainstream and west branch of the PIIS (Fig. 5) provides convenience for the invasion of the mCDW. The mCDW carries a large amount of heat into the ice cavity of the mainstream and west branch of the PIIS, causing serious basal melting. This is why ocean circulation mainly affects the mainstream and west branch of the PIIS (Dutrieux et al., 2014). The intrusion of mCDW promoted basal melting, resulting in a higher basal melt rate in mainstream of the PIIS. Local winds are an important factor in regulating the input of Amundsen Sea mCDW into the bottom of the PIIS (Dutrieux et al., 2014; Thoma et al., 2008; Steig et al., 2012). Changes in local winds can increase or decrease the volume transport of mCDW, thus affecting the heat exchange between ice shelf and ocean, promoting or inhibiting the basal melting. Additionally, local winds can drive the warm surface seawater into the bottom of the ice shelf to enhance heat exchange and thus promoting the basal

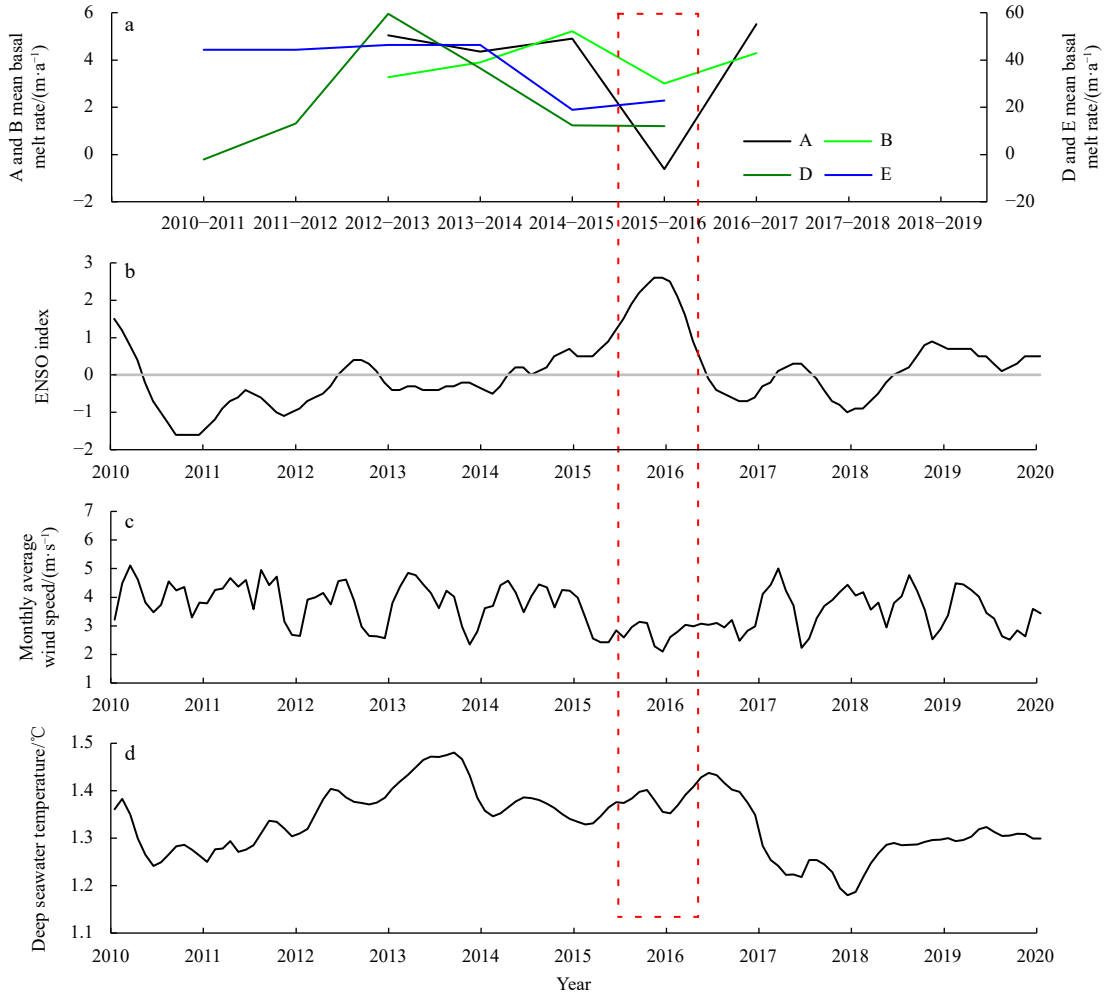


**Fig. 4.** Mean basal melt rate in small areas A, B, D and E, which are the same as the marks of the four specific locations in Fig. 1 (a); ENSO index (b); mean monthly wind speed around the PIIS (c); the deep water temperature at 880–1 000 m depth at the front of the PIIS from EN4 quality controlled ocean data (Good et al., 2013), which represents the temperature of mCDW (d).

melting of the ice shelf (Wang et al., 2020; Silvano et al., 2016).

The changes in the basal channels at locations C, D and E shown the same trend. From 2007 to 2010, both deep seawater temperature (Fig. 6b) and wind speed (Fig. 6a) have undergone a

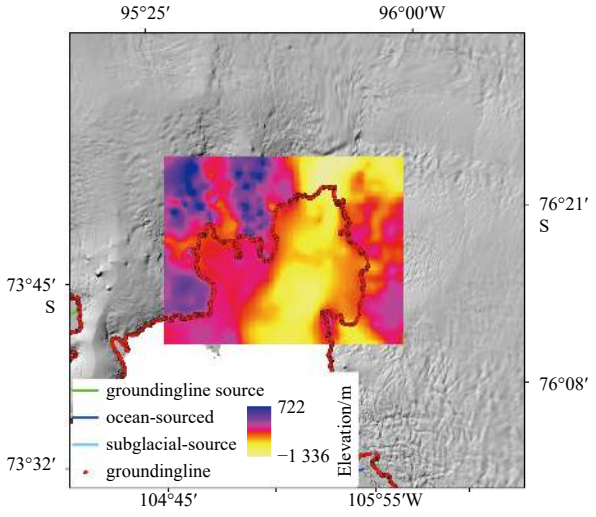


**Fig. 5.** Bedrock elevation of PIIS.

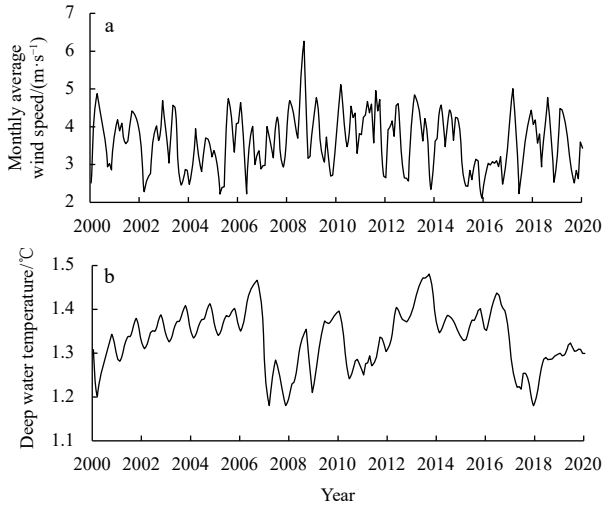


**Fig. 6.** Mean monthly wind speed around the PIIS from 2000 to 2020 (a); the deep water temperature at 880–1 000 m depth at the front of the PIIS from EN4 quality controlled ocean data (Good et al., 2013), which represents the temperature of mCDW from 2000 to 2020 (b).

significant increase, and the abnormal wind field (Fig. 7) also increased the CDW entering the bottom of the PIIS. Wind field and deep seawater temperature promoted the development of basal channels C, D and E, and reduce the surface elevations above basal channels C, D and E from 2007 to 2010. From 2010 to 2013, the temperature of deep seawater continued to rise (Fig. 6b), and

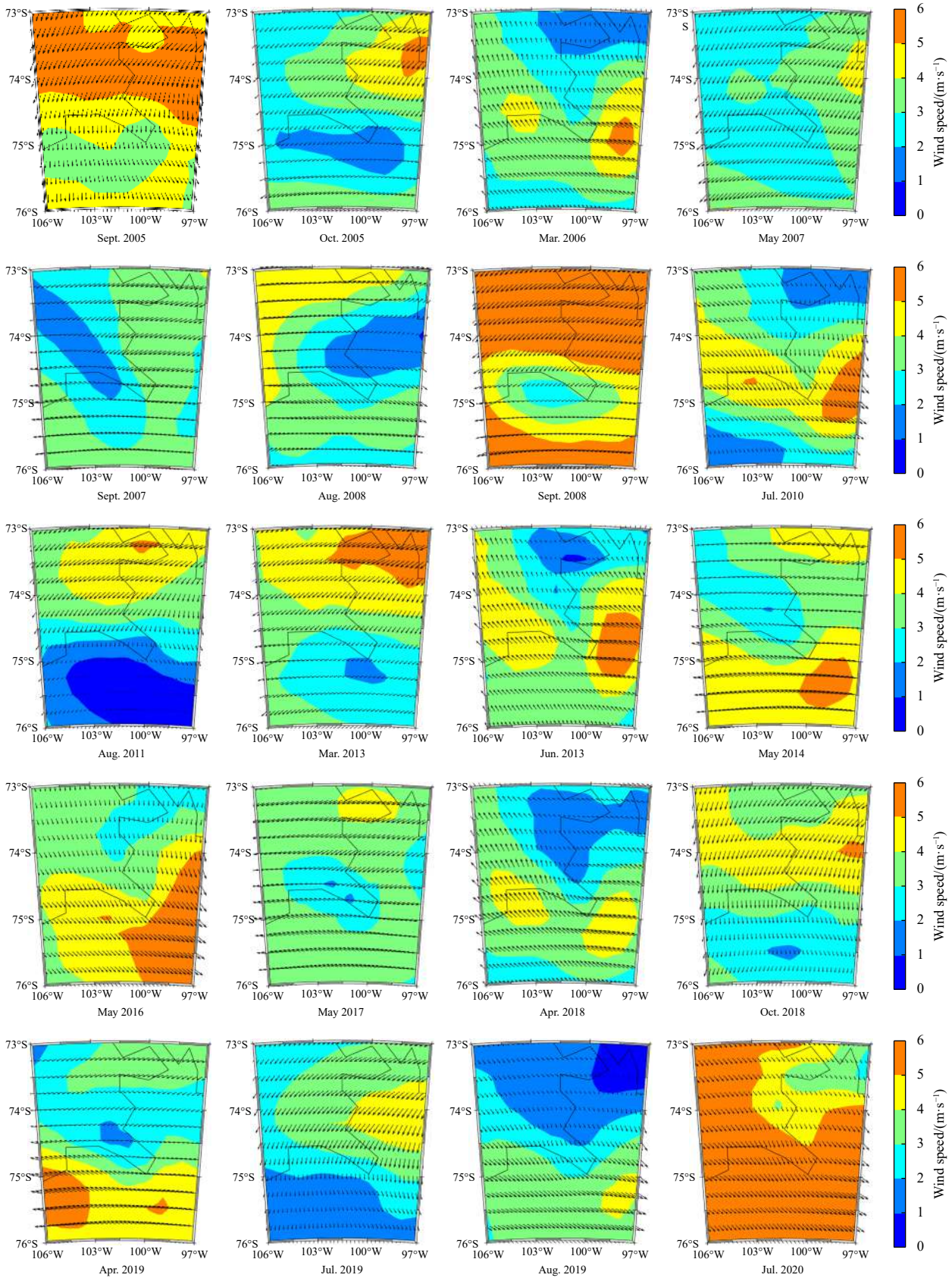


**Fig. 7.** Wind field in abnormal month surrounding the PIIS.

the wind speed was stable (Fig. 6a). Although there was a slight increase in both deep seawater temperature (Fig. 6b) and wind speed (Fig. 6a) between 2015 and 2018, the decreasing trend was still evident. The cooling CDW entering the bottom of the PIIS, which inhibited the development of the basal channels and increased the surface elevations above basal channels C, D and E. The change of wind field and deep seawater temperature were consistent with the changes of the surface elevations above basal channels C, D and E (Figs 2c–e). However, surface melting day (SMD) (Fig. 8) and SST (Fig. 9) did not show consistency with the surface elevations changes above basal channels C, D and E. Because the basal channels C and E are close to the groundingline, the basal channel D is far from the front edge of the PIIS, and the distance of interaction between the surface seawater and the bottom of the PIIS is not sufficient. Therefore, wind field and deep seawater temperature were the main factors affecting the surface elevation changes above basal channels C, D and E.

### 5.3 *West branch basal channel change*

The surface elevation changes above the basal channel F were similar to that of the basal channel D. The sustained cooling of CDW inhibited basal melting of the PIIS in 2014 and 2015. However, surface melting day on the PIIS only occurred for 8 d in 2014 (Fig. 8), and the lower atmospheric temperature on the surface can also cause surface freezing of the basal channel F surface. The cooling CDW and lower surface atmospheric temperature inhibited the development of the basal channel, resulting in the maximum surface elevation above the basal channel F. The number of surface melting days in both 2007 and 2016 was several tens of days (Fig. 8). The higher surface atmospheric temperature can also cause surface melting of the PIIS, and the higher SST in the same year (Fig. 9) can promote the development of the basal channel. Therefore, the surface elevation changes above the basal channel F was minimized due to the rise of surface atmospheric temperature and SST.

### 5.4 *ENSO regulates basal melt rate*

The basal melt rates of the east branch of the PIIS were 0–6 m/a. The maximum mean basal melt rate of the mainstream of the PIIS was about 50 m/a, which was consistent with the simulation results of Bradley et al. (2022), seriously weakening the stability of the PIIS. The seabed topography at the front of the PIIS is the main factor causing regional differences in basal melting. The mean basal melt rate first increased and then decreased from 2010–2011 to 2015–2016 with the mean reduction was 34%, and shown an obvious law of time change. Especially in 2015–2016, the basal melt rate reached its lowest value. The westerly wind in the surface of Amundsen Sea increased the transport of mCDW/CDW and surface seawater into the bottom of the PIIS, and the temperature increased and accelerated the basal melting (Silvano et al., 2016; Dotto et al., 2019). The SST around the PIIS (Fig. 9) and the deep seawater temperature (Fig. 4d) shown a trend of first increased and then decreased, which was consistent with the change trend of the mean basal melt rate. Therefore, SST and deep seawater temperature affected basal melting of the PIIS.

SST, wind field and deep seawater temperature can affect the basal melting of the ice shelf, while SST, wind field and deep seawater temperature are affected by El Niño/Southern Oscillation (ENSO). ENSO can cause most of the observed variability in the atmosphere, ocean and sea ice in the Amundsen–Bellingshausen seas sector (Kerr and McConnochie, 2015; Good et al., 2013). Regional responses to ENSO surface air temperature and upwelling of CDW near the front of Pine Island Glacier's ice shelf have been observed (Dutrieux et al., 2014; Paolo et al., 2018). To investigate the climate drivers of the reduction of basal melt rate in 2015–2016, we analyzed the geopotential height anomalies of 500 hPa over Antarctica and annual-mean wind at front of PIIS using ERA5 reanalysis data. Figure 10a and b showed the mean geopotential height anomalies at 500 hPa and mean wind speed vectors for three periods. They are also corresponding to La Niña, normal climate, and El Niño. Especially the 2015–2016 period corresponds to the 2015 extreme El Niño event (Figs 4b and 10a). Changes in the pressure of the Pacific sector and the Antarctic continental shelf can lead to significant changes in the wind field, and unusual mean easterly winds occur during this period (Fig. 10b). Therefore, unusual mean westerly winds occur during this period (Fig. 10b). El Niño (La Niña) can change the pressure and wind field in the Amundsen Sea, thereby affecting the changes in its surrounding ice shelves (Dutrieux et al., 2014; Paolo et al., 2018).

Although the westerly winds promoted CDW into the bottom of the PIIS during the El Niño period (2015–2016) compared to normal and La Niña (Fig. 10b), while wind speed (Fig. 4c) and deep seawater temperature (Fig. 4d) showed a decreasing trend. This restrained basal melting of the PIIS, causing the basal melt rate reached its lowest value in 2015–2016. Paolo at el. (2018) also confirmed this point that there was no significant increase in the

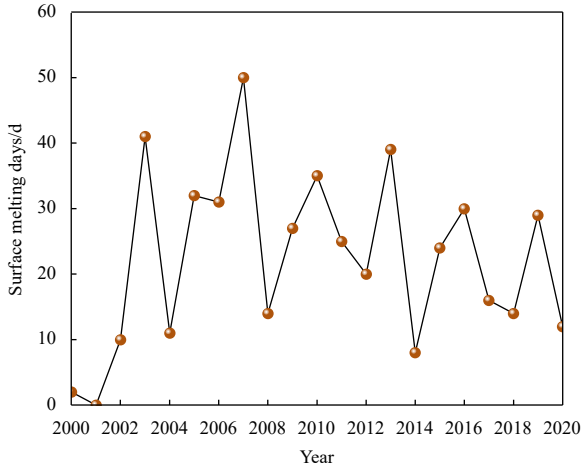


**Fig. 8.** Surface melting days of the PIIS.

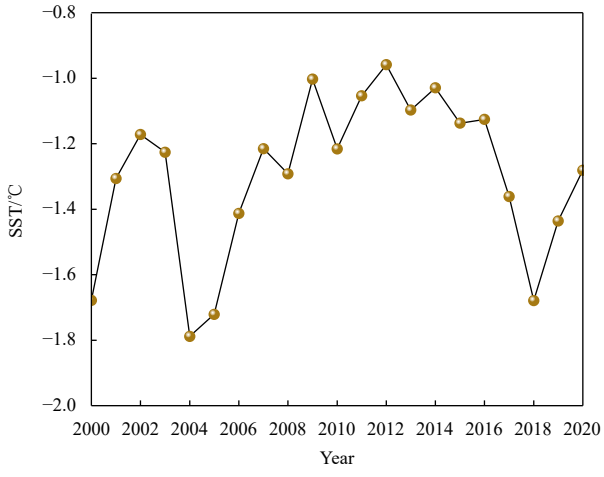


**Fig. 9.** SST at the front end of the PIIS. Annual mean from 2000 to 2020.

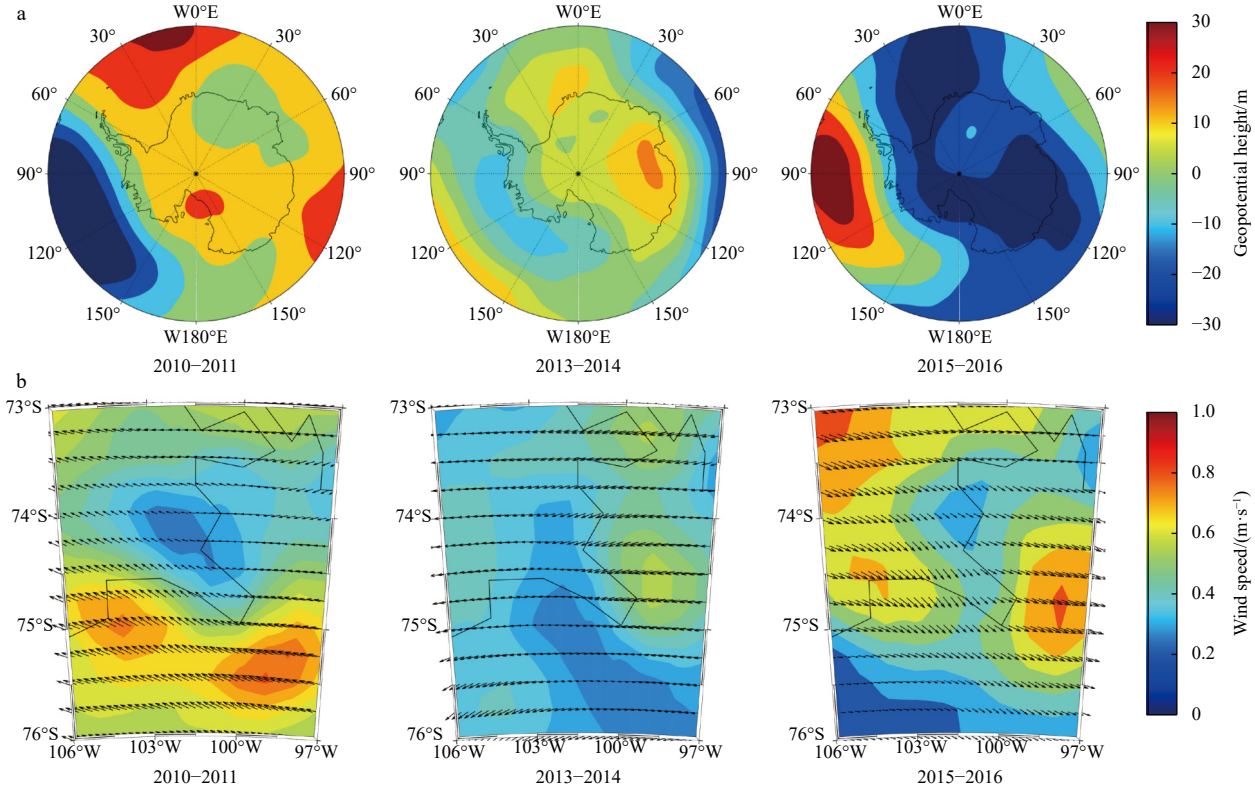


**Fig. 10.** Annual-mean anomalies in atmospheric for 2010–2011 (left), 2013–2014 (mid) and 2015–2016 (right). a. ERA5 biennial mean geopotential height at 500 hPa; b. ERA5 biennial mean wind speed vectors.

basal melting of the PIIS between 2015 and 2016. However, the mean basal melt rates at the basal channels were relatively large and changes steadily during periods when there is no El Niño event influence (Fig. 4a). On the contrary, La Niña event occurred in 2010–2011 (Fig. 4b), and the atmospheric environment was opposite to El Niño. According to the current calculation results, it was also found that the basal melt rate was higher in 2010–2011. However, the current observation data was limited, we need to further increase the long-term calculation to support the impact of La Niña event on the basal melting.

## 6 Conclusions

Our results provided more about the coupling relationship between Pine Island Ice Shelf (PIIS) and atmosphere or ocean. The fusion of surface elevation data from multiple sources allow us to examine the surface elevation changes above the basal channels over large areas with high spatial detail basal melt rate in Eulerian frameworks. Our results have shown that the basal channels network system of the PIIS is well-developed, with three types of channels present and a total length of over 450 km. Our long time series of observations have shown that the surface elevation changes above east branch the basal channels were relatively stable, the surface elevation changes above mainstream and west branch were significant, and were respectively affected by deep seawater temperature, wind field, SST and surface melting. The basal melt rate of east branch was relatively small, and the mean basal melt rate was 0–6 m/a. Mainstream basal melt rate was relatively large, and the highest mean basal melt rate was close to 50 m/a. The mean basal melt rate first increased and then decreased between 2010–2011 and 2015–2016, which was mainly due to the combined effect of SST, deep seawater temperature, and wind field. However, these factors were affected by the ENSO, the biennial mean geopotential height at 500 hPa also suggested that ENSO was the main driver of the observed changes in the basal melting of the PIIS. Therefore, the seabed topography has led to difference in basal melting of different areas of the PIIS. ENSO affected basal melting of the PIIS in the time scale.

***Acknowledgements***

The wind data are available at European Centre for Medium-Range Weather Forecasts (https://cds.climate.copernicus.eu/). The IceBridge data are available at National Snow and Ice Data Center (https://nsidc.org/data/IRMCR2/versions/1). The ICESat-1 data are available at National Snow and Ice Data Center (https://nsidc.org/data/glah12). The ICESat-2 data are available at National Snow and Ice Data Center (https://nsidc.org/data/ATL06/versions/4). The REMA DEM data are available at https://www.pgc.umn.edu/data/rema/. The LandSat data for this research are from United States Geological Survey (https://earthexplorer.usgs.gov/). The SMD data for this research are from http://pp.ige-grenoble.fr/pageperso/picardgh/melting/. The SMB data for this research are from https://www.projects.science.uu.nl/iceclimate/publications/data/2018/vwessem2018_tc/RACMO_Yearly/. The ice velocity data for this research are from National Snow and Ice Data Center (http://nsidc.org/apps/itslive/). The SST data for this research are from Met Office Hadley Center (https://www.metoffice.gov.uk/hadobs/hadsst3/data/download.html). The ENSO indices for this research are from https://origin.cpc.ncep.noaa.gov/products/analysis_monitoring/ensostuff/ONI_v5.php.

## References

Adusumilli S, Fricker H A, Siegfried M R, et al. 2018. Variable basal melt rates of Antarctic Peninsula ice shelves, 1994–2016. Geo-

physical Research Letters, 45(9): 4086–4095, doi: 10.1002/2017GL076652
Alley R B, Clark P U, Huybrechts P, et al. 2005. Ice-sheet and sea-level changes. Science, 310(5747): 456–460, doi: 10.1126/science.1114613
Alley K E, Scambos T A, Siegfried M R, et al. 2016. Impacts of warm water on Antarctic ice shelf stability through basal channel formation. Nature Geoscience, 9(4): 290–293, doi: 10.1038/ngeo2675
Bindschadler R, Vaughan D G, Vornberger P. 2011. Variability of basal melt beneath the Pine Island Glacier ice shelf, West Antarctica. Journal of Glaciology, 57(204): 581–595, doi: 10.3189/002214311797409802
Bintanja R, van Oldenborgh G J, Drijfhout S S, et al. 2013. Important role for ocean warming and increased ice-shelf melt in Antarctic sea-ice expansion. Nature Geoscience, 6(5): 376–379, doi: 10.1038/ngeo1767
Borsa A A, Moholdt G, Fricker H A, et al. 2014. A range correction for ICESat and its potential impact on ice-sheet mass balance studies. The Cryosphere, 8(2): 345–357, doi: 10.5194/tc-8-345-2014
Bradley A T, Bett D T, Dutrieux P, et al. 2022. The influence of Pine Island Ice Shelf calving on basal melting. Journal of Geophysical Research: Oceans, 127(9): e2022JC018621, doi: 10.1029/2022JC018621
Chartrand A M, Howat I M. 2020. Basal channel evolution on the Getz ice shelf, west Antarctica. Journal of Geophysical Research: Earth Surface, 125(9): e2019JF005293, doi: 10.1029/2019JF005293
Cornford S L, Martin D F, Payne A J, et al. 2015. Century-scale simulations of the response of the West Antarctic Ice Sheet to a warming climate. The Cryosphere, 9(4): 1579–1600, doi: 10.5194/tc-9-1579-2015
Davis P E D, Jenkins A, Nicholls K W, et al. 2018. Variability in basal melting beneath Pine Island Ice Shelf on weekly to monthly timescales. Journal of Geophysical Research: Oceans, 123(11): 8655–8669, doi: 10.1029/2018JC014464
De Rydt J, Holland P R, Dutrieux P, et al. 2014. Geometric and oceanographic controls on melting beneath Pine Island Glacier. Journal of Geophysical Research: Oceans, 119(4): 2420–2438, doi: 10.1002/2013JC009513
Dotto T S, Garabato A C N, Bacon S, et al. 2019. Wind-driven processes controlling oceanic heat delivery to the Amundsen Sea, Antarctica. Journal of Physical Oceanography, 49(11): 2829–2849, doi: 10.1175/JPO-D-19-0064.1
Dutrieux P, De Rydt J, Jenkins A, et al. 2014. Strong sensitivity of Pine Island ice-shelf melting to climatic variability. Science, 343(6167): 174–178, doi: 10.1126/science.1244341
Farrell S L, Kurtz N, Connor L N, et al. 2012. A first assessment of IceBridge snow and ice thickness data over Arctic sea ice. IEEE Transactions on Geoscience and Remote Sensing, 50(6): 2098–2111, doi: 10.1109/TGRS.2011.2170843
Favier L, Durand G, Cornford S L, et al. 2014. Retreat of Pine Island Glacier controlled by marine ice-sheet instability. Nature Climate Change, 4(2): 117–121, doi: 10.1038/nclimate2094
Fricker H A, Padman L. 2006. Ice shelf grounding zone structure from ICESat laser altimetry. Geophysical Research Letters, 33(15): L15502, doi: 10.1029/2006gl026907
Fricker H A, Padman L. 2012. Thirty years of elevation change on Antarctic Peninsula ice shelves from multi mission satellite radar altimetry. Journal of Geophysical Research: Oceans, 117(C2): C02026, doi: 10.1029/2011JC007126
Gardner A S, Fahnestock M A, Scambos T A. 2019. [update to time of data download]: MEaSUREs ITS_LIVE landsat image-pair glacier and ice sheet surface velocities: version 1. Data archived at National Snow and Ice Data Center, doi: 10.5067/IMR9D3PEI28U, https://its-live.jpl.nasa.gov/[2023-01-23]
Good S A, Martin M J, Rayner N A. 2013. EN4: quality controlled ocean temperature and salinity profiles and monthly objective analyses with uncertainty estimates. Journal of Geophysical Research: Oceans, 118(12): 6704–6716, doi: 10.1002/2013JC009067
Goward S N, Masek J G, Williams D L, et al. 2001. The Landsat 7 mission: terrestrial research and applications for the 21st century. Remote Sensing of Environment, 78(1–2): 3–12, doi: 10.1016/S0034-4257(01)00262-0
Gregg M C. 1987. Diapycnal mixing in the thermocline: a review. Journal of Geophysical Research: Oceans, 92(C5): 5249–5286, doi: 10.1029/JC092iC05p05249
Hersbach H, Bell B, Berrisford P, et al. 2019. ERA5 monthly averaged data on single levels from 1979 to present. Copernicus Climate Change Service (C3S) Climate Data Store (CDS), 10: 24381
Howat I M, Porter C, Smith B E, et al. 2019. The reference elevation model of Antarctica. The Cryosphere, 13(2): 665–674, doi: 10.5194/tc-13-665-2019
Jacobs S S, Hellmer H H, Jenkins A. 1996. Antarctic ice sheet melting in the southeast Pacific. Geophysical Research Letters, 23(9): 957–960, doi: 10.1029/96GL00723
Joughin I, Smith B E, Holland D M. 2010. Sensitivity of 21st century sea level to ocean-induced thinning of Pine Island Glacier, Antarctica. Geophysical Research Letters, 37(20): L20502, doi: 10.1029/2010GL044819
Joughin I, Smith B E, Medley B. 2014. Marine ice sheet collapse potentially under way for the Thwaites Glacier Basin, West Antarctica. Science, 344(6185): 735–738, doi: 10.1126/science.1249055
Joughin I, Smith B E, Schoof C G. 2019. Regularized coulomb friction laws for ice sheet sliding: application to Pine Island Glacier, Antarctica. Geophysical Research Letters, 46(9): 4764–4771, doi: 10.1029/2019GL082526
Kerr R C, McConnochie C D. 2015. Dissolution of a vertical solid surface by turbulent compositional convection. Journal of Fluid Mechanics, 765: 211–228, doi: 10.1017/jfm.2014.722
Kurtz N T, Farrell S L. 2011. Large-scale surveys of snow depth on Arctic sea ice from Operation IceBridge. Geophysical Research Letters, 38(20): L20505, doi: 10.1029/2011GL049216
Liang Qi, Zhou Chunxia, Zheng Lei. 2021. Mapping basal melt under the Shackleton ice shelf, East Antarctica, from CryoSat-2 radar altimetry. IEEE Journal of Selected Topics in Applied Earth Observations and Remote Sensing, 14: 5091–5099, doi: 10.1109/JSTARS.2021.3077359
Ligtenberg S R M, Kuipers Munneke P, van den Broeke M R. 2014. Present and future variations in Antarctic firn air content. The Cryosphere, 8(5): 1711–1723, doi: 10.5194/tc-8-1711-2014
Liu Yan, Moore J C, Cheng Xiao, et al. 2015. Ocean-driven thinning enhances iceberg calving and retreat of Antarctic ice shelves. Proceedings of the National Academy of Sciences of the United States of America, 112(11): 3263–3268, doi: 10.1073/pnas.1415137112
Liu Zhiwei, Zhu Jianjun, Fu Haiqiang, et al. 2020. Evaluation of the vertical accuracy of open global DEMs over steep terrain regions using ICESat data: a case study over Hunan Province, China. Sensors, 20(17): 4865, doi: 10.3390/s20174865
Logan L, Catania G, Lavier L, et al. 2013. A novel method for predicting fracture in floating ice. Journal of Glaciology, 59(216): 750–758, doi: 10.3189/2013JoG12J210
Markus T, Neumann T, Martino A, et al. 2017. The Ice, Cloud, and land Elevation Satellite-2 (ICESat-2): science requirements, concept, and implementation. Remote Sensing of Environment, 190: 260–273, doi: 10.1016/j.rse.2016.12.029
McGrath D, Steffen K, Rajaram H, et al. 2012. Basal crevasses on the Larsen C Ice Shelf, Antarctica: implications for meltwater ponding and hydrofracture. Geophysical Research Letters, 39(16): L16504, doi: 10.1029/2012GL052413
Moholdt G, Padman L, Fricker H A. 2014. Basal mass budget of Ross and Filchner-Ronne ice shelves, Antarctica, derived from Lagrangian analysis of ICESat altimetry. Journal of Geophysical Research: Earth Surface, 119(11): 2361–2380, doi: 10.1002/2014JF003171
Morlighem M, Rignot E J, Binder T, et al. 2018. BedMachine Antarctica v1: a new subglacial bed topography and ocean bathymetry dataset of Antarctica combining mass conservation, gravity inversion and streamline diffusion. In: Proceedings of the American Geophysical Union, Fall Meeting 2018. Washing-

ton: AGU
Nias I J, Cornford S L, Payne A J. 2016. Contrasting the modelled sensitivity of the Amundsen Sea Embayment ice streams. Journal of Glaciology, 62(233): 552–562, doi: 10.1017/jog.2016.40
Noh M J, Howat I M. 2017. The surface extraction from TIN based search-space minimization (SETSM) algorithm. ISPRS Journal of Photogrammetry and Remote Sensing, 129: 55–76, doi: 10.1016/j.isprsjprs.2017.04.019
Paolo F S, Fricker H A, Padman L. 2015. Volume loss from Antarctic ice shelves is accelerating. Science, 348(6232): 327–331, doi: 10.1126/science.aaa0940
Paolo F S, Padman L, Fricker H A, et al. 2018. Response of Pacific-sector Antarctic ice shelves to the El Niño/Southern oscillation. Nature Geoscience, 11(2): 121–126, doi: 10.1038/s41561-017-0033-0
Payne A J, Vieli A, Shepherd A P, et al. 2004. Recent dramatic thinning of largest West Antarctic ice stream triggered by oceans. Geophysical Research Letters, 31(23): L23401, doi: 10.1029/2004GL021284
Pritchard H D, Ligtenberg S R M, Fricker H A, et al. 2012. Antarctic ice-sheet loss driven by basal melting of ice shelves. Nature, 484(7395): 502–505, doi: 10.1038/nature10968
Rignot E, Mouginot J, Scheuchl B, et al. 2019. Four decades of Antarctic Ice Sheet mass balance from 1979–2017. Proceedings of the National Academy of Sciences of the United States of America, 116(4): 1095–1103, doi: 10.1073/pnas.1812883116
Rignot E, Steffen K. 2008. Channelized bottom melting and stability of floating ice shelves. Geophysical Research Letters, 35(2): L02503, doi: 10.1029/2007GL031765
Rosevear M G, Gayen B, Galton-Fenzi B K. 2022. Regimes and transitions in the basal melting of Antarctic ice shelves. Journal of Physical Oceanography, 52(10): 2589–2608, doi: 10.1175/JPO-D-21-0317.1
Roy D P, Wulder M A, Loveland T R, et al. 2014. Landsat-8: science and product vision for terrestrial global change research. Remote Sensing of Environment, 145: 154–172, doi: 10.1016/j.rse.2014.02.001
Schmidt B E, Washam P, Davis P E D, et al. 2023. Heterogeneous melting near the Thwaites Glacier groundingline. Nature, 614(7948): 471–478, doi: 10.1038/s41586-022-05691-0
Seroussi H, Morlighem M, Rignot E, et al. 2014. Sensitivity of the dynamics of Pine Island Glacier, West Antarctica, to climate forcing for the next 50 years. The Cryosphere, 8(5): 1699–1710, doi: 10.5194/tc-8-1699-2014
Seroussi H, Nakayama Y, Larour E, et al. 2017. Continued retreat of Thwaites Glacier, West Antarctica, controlled by bed topography and ocean circulation. Geophysical Research Letters, 44(12): 6191–6199, doi: 10.1002/2017GL072910
Shean D E, Joughin I R, Dutrieux P, et al. 2019. Ice shelf basal melt rates from a high-resolution digital elevation model (DEM) record for Pine Island Glacier, Antarctica. The Cryosphere, 13(10): 2633–2656, doi: 10.5194/tc-13-2633-2019
Shepherd A, Fricker H A, Farrell S L. 2018. Trends and connections across the Antarctic cryosphere. Nature, 558(7709): 223–232, doi: 10.1038/s41586-018-0171-6
Shepherd A, Wingham D, Payne T, et al. 2003. Larsen ice shelf has progressively thinned. Science, 302(5646): 856–859, doi: 10.1126/science.1089768
Silvano A, Rintoul S R, Herraiz-Borreguero L. 2016. Ocean-ice shelf interaction in East Antarctica. Oceanography, 29(4): 130–143, doi: 10.5670/oceanog.2016.105
Stanton T P, Shaw W J, Truffer M, et al. 2013. Channelized ice melting in the ocean boundary layer beneath Pine Island Glacier, Antarctica. Science, 341(6151): 1236–1239, doi: 10.1126/science.1239373
Steig E J, Ding Q, Battisti D S, et al. 2012. Tropical forcing of Circumpolar Deep Water inflow and outlet glacier thinning in the Amundsen Sea Embayment, West Antarctica. Annals of Glaciology, 53(60): 19–28, doi: 10.3189/2012AoG60A110
Suga Y, Ogawa H, Ohno K, et al. 2003. Detection of surface temperature from Landsat-7/ETM+. Advances in Space Research, 32(11): 2235–2240, doi: 10.1016/S0273-1177(03)90548-5
Tang Chengjia, Li Yuansheng, Chen Zhenlou, et al. 2008. A review on studies of Antarctic ice shelves and advances in Chinese research on Amery ice shelf. Chinese Journal of Polar Research (in Chinese), 20(3): 265–274
Thoma M, Jenkins A, Holland D, et al. 2008. Modelling circumpolar deep water intrusions on the Amundsen Sea continental shelf, Antarctica. Geophysical Research Letters, 35(18): L18602, doi: 10.1029/2008GL034939
van Wessem J M, van de Berg W J, Noël B P Y, et al. 2018. Modelling the climate and surface mass balance of polar ice sheets using RACMO2–Part 2: Antarctica (1979–2016). The Cryosphere, 12(4): 1479–1498, doi: 10.5194/tc-12-1479-2018
Vaughan D G, Corr H F J, Bindschadler R A, et al. 2012. Subglacial melt channels and fracture in the floating part of Pine Island Glacier, Antarctica. Journal of Geophysical Research: Earth Surface, 117(F3): F03012, doi: 10.1029/2012JF002360
Vermote E, Justice C, Claverie M, et al. 2016. Preliminary analysis of the performance of the Landsat 8/OLI land surface reflectance product. Remote Sensing of Environment, 185: 46–56, doi: 10.1016/j.rse.2016.04.008
Wåhlin A K, Yuan X, Björk G, et al. 2010. Inflow of warm circumpolar deep water in the central Amundsen shelf. Journal of Physical Oceanography, 40(6): 1427–1434, doi: 10.1175/2010JPO4431.1
Walker D P, Jenkins A, Assmann K M, et al. 2013. Oceanographic observations at the shelf break of the Amundsen Sea, Antarctica. Journal of Geophysical Research: Oceans, 118(6): 2906–2918, doi: 10.1002/jgrc.20212
Wang Xianwei, Gong Peng, Zhao Yuanyuan, et al. 2013. Water-level changes in China's large lakes determined from ICESat/GLAS data. Remote Sensing of Environment, 132: 131–144, doi: 10.1016/j.rse.2013.01.005
Wang Zemin, Song Xiangyu, Zhang Baojun, et al. 2020. Basal channel extraction and variation analysis of Nioghalvfjerdsfjorden ice shelf in Greenland. Remote Sensing, 12(9): 1474, doi: 10.3390/rs12091474
WCRP Global Sea Level Budget Group. 2018. Global sea-level budget 1993-present. Earth System Science Data, 10(3): 1551–1590, doi: 10.5194/essd-10-1551-2018